Engineering 60 (2026) 166–176

Contents lists available at ScienceDirect

Engineering

journal homepage: www.elsevier.com/locate/eng

Research
Material Science and Engineering—Article

Investigating the Spectroscopic Performance of $Y_3Al_5O_{12}:Mn^{4+}$ Phosphors Co-Doped with Divalent Metal Ions and the Use of Phosphor Film for "Green" Plant Cultivation

Fen Wang [a,b], Hirohisa Miyata [b], Jingyi Liang [a], Yingying Song [c], Guangyuan Xu [c], Jumpei Ueda [b,*], Dan Wang [a,*]

[a] State Key Laboratory of Organic–Inorganic Composites, College of Chemical Engineering, Beijing University of Chemical Technology, Beijing 100029, China
[b] Graduate School of Advanced Science and Technology, Japan Advanced Institute of Science and Technology, Nomi 923-1292, Japan
[c] State Key Laboratory of Agricultural and Forestry Biosecurity, MOA Key Lab of Pest Monitoring and Green Management, College of Plant Protection, China Agricultural University, Beijing 100193, China

ARTICLE INFO

Article history:
Received 31 March 2025
Revised 1 August 2025
Accepted 2 September 2025
Available online 15 April 2026

Keywords:
Phosphors
Light-conversion agents
Plant cultivation

ABSTRACT

The intensity and quality of the artificial light used in "green" plant cultivation greatly affect plant morphogenesis and physiological responses. Light-conversion films based on phosphors that can enable the precise conversion of ultraviolet (UV) radiation into photosynthetically active radiation (i.e., red light) hold great promise for next-generation ecological agriculture. However, conventional red phosphors often suffer from low stability or emit a short-wavelength red light more suitable for display than plant growth, limiting their agricultural applications. Herein, a weather-resistant Mn^{4+}-doped yttrium aluminum garnet (YAG:Mn^{4+}) deep red phosphor with a strong emission peak at 672 nm was synthesized. The phosphor's luminescent properties were optimized by introducing Mg^{2+} as a charge compensator, thereby significantly increasing the phosphor's emission intensity. Detailed photoluminescence and thermal quenching behaviors were investigated through comprehensive spectroscopic analyses. Light-conversion film made of biodegradable polyvinyl alcohol and the prepared phosphors was utilized to intensify the process of cultivating pea seedlings. As a proof of concept, a preliminary study under sunlight with an additional UV lamp demonstrated that treatment with the prepared light-conversion film enhanced the growth of pea seedlings. These improvements can be attributed to the effective conversion of UV radiation, which is useless for plant growth, into beneficial red light. The results demonstrate the potential of YAG:Mn^{4+}–Mg^{2+}-based phosphor films to improve agricultural productivity and promote eco-friendly cultivation practices.

1. Introduction

Photosynthesis is the basis of agricultural production, and the essence of photosynthesis is a chemical transformation process driven by light energy in which sunlight is absorbed to synthesize energy-rich compounds from water and carbon dioxide (CO_2), which are then used to produce the biomass of living organisms [1–3]. As the human population continues to grow rapidly, increasing requirements for food, materials, and energy have created a need to increase both the amount of photosynthesis occurring and the efficiency of converting photosynthetic output into products useful to people [4–6]. Light is the most important environmental factor for agricultural production, as it not only provides energy for photosynthesis but also acts as a modulating signal for many aspects of plant growth and reproduction [7,8]. Research has shown that photons of different wavelengths in sunlight have significantly different botanical effects, affecting plants' morphological structure [9], chemical composition [10,11], photosynthesis [12,13], and organ growth [9,14,15]. For example, a study on the effects of light-emitting diode (LED) light supplementation on strawberries concluded that red light induces the highest plant productivity and targets anthocyanin accumulation, whereas blue

* Corresponding authors.
E-mail addresses: ueda-j@jaist.ac.jp (J. Ueda), wangdan@mail.buct.edu.cn (D. Wang).

https://doi.org/10.1016/j.eng.2025.09.035

and green light increase the accumulation of primary and secondary metabolites [16]. Based on intelligent regulatory systems, modern agriculture can precisely regulate the wavelength and intensity of the light reaching crops, optimize nutrition through various nutrient solutions, and make full use of solar energy [17] to stimulate plant growth and increase its nutritional value. In this way, agriculture is liberated from complete dependence on the natural environment, opening up a new world of science and technology for agricultural production [18].

The use of light-conversion film can play a dual role, both acting as an ordinary agricultural film to preserve moisture and heat and converting the portion of natural solar radiation useless for plant growth into light that promotes plant growth, without any other energy inputs [15,19]. For producing an excellent light-conversion film, light-conversion materials that are extremely weather-proof and have the desired optical properties and no toxicity are ideal [20]. At present, Eu^{2+}-doped nitride phosphors are the most mature red-light-emitting materials, with high quantum efficiency and a high quenching temperature. However, the preparation of nitride phosphors requires harsh conditions, usually being carried out in an inert gas atmosphere or even under high temperatures or pressures [21,22]. The transition metal ion Mn^{4+} has been considered as a promising red-emission luminescent center, and fluoride phosphor doped with Mn^{4+} successfully achieves the deep red emission required by plants, with a quantum efficiency of more than 95% [23,24]. However, toxic hydrofluoric acid (HF) is used in the preparation process of this phosphor; moreover, the phosphor is unstable under high humidity, generating toxic HF, which limits its application in agriculture [25,26]. In recent years, Mn^{4+}-doped oxide phosphors have attracted attention for their simple preparation process and high environmental stability [22,27]. Among oxide phosphors, the structure of yttrium aluminum garnet (YAG) is stable from a chemical and photochemical point of view, and phosphors possessing this structure generally show high stability [28–30]. In addition, the ionic radius of Mn^{4+} (0.53 Å) is similar to that of the aluminum (Al) in YAG (0.535 Å), which has an octahedral geometry (coordination number (CN) = 6); thus, Mn^{4+} can be doped into YAG and remain stable [31]. Since Al^{3+} and Mn^{4+} have different valence states, charge compensation is required. To achieve this, some of the doped manganese (Mn) ions may be reduced to a trivalent state, although this weakens the luminescence intensity of the phosphor [31,32]. Thus far, several charge compensators have been studied for use in stabilizing Mn^{4+} ions and improving the luminescent properties of Mn^{4+}-doped phosphors [27,31].

In this work, various divalent metal ions (M^{2+}, where M = Mg, Zn, Ca, or Ba) were co-doped into YAG:Mn^{4+} as a charge compensator in order to improve the phosphor's luminescent properties. Based on the results, the effects of the doping sites (i.e., the dodecahedral Y^{3+} site or the octahedral Al^{3+} site) of M^{2+} in terms of the resulting luminescent properties were investigated. The phosphors were synthesized in sub-micron particles using a sol–gel method to prepare a uniform luminescent film. The most efficient phosphors, which have a red emission peak at 672 nm when excited in a wide wavelength range from ultraviolet (UV) to green light, were obtained by substituting Al^{3+} with Mg^{2+}. This YAG:Mn^{4+}–Mg^{2+} deep red phosphor was investigated in detail using low-temperature spectroscopy, vacuum ultraviolet (VUV) spectroscopy, chemical durability testing, and so forth. The YAG:Mn^{4+}–Mg^{2+} phosphor maintained intensities of 73%, 88%, and 78% with respect to the original luminescence intensity after being immersed in deionized water for 15 d, treated with acid for 5 h, and treated with alkali for 5 h, respectively. The YAG:Mn^{4+}–Mg^{2+} phosphor was also mixed with biodegradable polyvinyl alcohol (PVA) [33] to form a light-conversion film that absorbed the useless UV and green bands of the natural solar spectrum and emitted the deep red light favorable to photosynthesis. The prepared film was used in the growing process of pea seedlings, using conditions similar to those reported previously [34,35]. The height of the pea seedlings above the root, their fresh weight, and their β-carotene content increased by 41.3%, 39.0%, and 14.22%, respectively, after treatment with the light-conversion film.

2. Experimental procedure

2.1. Materials

The raw materials used to obtain the $Y_3Al_5O_{12}$ (YAG) host were $Al(NO_3)_3{\cdot}9H_2O$ and $Y(NO_3)_3{\cdot}6H_2O$. Samples with different concentrations of Mn^{4+}—that is, YAG:$m$$Mn^{4+}$ (m = 0.05%, 0.1%, 0.2%, and 0.3% for the octahedral site)—were prepared by doping Mn into the YAG host, for which the Mn source was $Mn(NO_3)_2{\cdot}4H_2O$. The YAG was co-doped with Mg^{2+}, Zn^{2+}, Ca^{2+}, or Ba^{2+} as a charge compensator to optimize its luminescence. The following samples were prepared: YAG:Mn^{4+}–$n$$Mg^{2+}$ (n = 0%, 2%, 4%, and 8% for the octahedral site). The $Al(NO_3)_3{\cdot}9H_2O$, $Y(NO_3)_3{\cdot}6H_2O$, $Mn(NO_3)_2{\cdot}4H_2O$, $Mg(NO_3)_2{\cdot}6H_2O$, $Zn(NO_3)_2{\cdot}6H_2O$, $Ca(NO_3)_2{\cdot}4H_2O$, $BaCl_2{\cdot}2H_2O$, and citric acid were purchased from Shanghai Maclin Biochemical Technology Co., Ltd. (China); all these chemicals had a trace metal purity of 99.9%. PVA with an average degree of aggregation of 1750 ± 50 was purchased from Shanghai Yuanye Bio-Technology Co., Ltd. (China). All chemicals were used without any additional purification, unless otherwise mentioned.

2.2. Synthesis of the phosphors

The garnet matrix phosphors were prepared by means of the sol–gel method [36], with a molar ratio of citric acid to metal cations of 1.5:1.0. In brief, a solution of citric acid with a concentration of 0.72 mol·L^{-1} and a nitrate solution with a total metal cation concentration of 0.48 mol·L^{-1} were prepared. These two solutions were then mixed and heated at 75 °C for 6 h to obtain a yellowish sol. The sol was placed in an oven and dried at 120 °C for 12 h to obtain a loose and porous dry gel. Finally, the dry gel powder was calcined at 1200 °C for 4 h in a muffle furnace to obtain the phosphors.

2.3. Preparation of the light-conversion film

In this work, biodegradable PVA was selected as the film material. Two grams of PVA were added to 20 mL of deionized water and heated in a water bath at 95 °C with stirring until completely dissolved. A certain amount of red phosphor, as prepared in the previous step, was then added to this aqueous PVA solution, and the mixture was stirred continuously for 1 h. The mixture was placed in a Teflon mold and left at room temperature to remove bubbles and water, yielding the light-conversion film.

2.4. Cultivation of pea seedlings under the light-conversion film

In this work, pea seedlings—a common vegetable—were selected as the sample, and the influence of light on the seedlings' growth was investigated. In the experiment, the pea seedlings were maintained in the same environment, including water, temperature (maintained at (25 ± 1) °C), and other factors, to avoid unnecessary influences aside from the changes in lighting. As a proof of concept, an additional UV lamp (6 W, emission range 300–400 nm, peak at 365 nm) was used for both groups to make the eventual difference between them more apparent. The exposure duration was set at 24 h per day for 8 consecutive days. The light-conversion film was placed between the pea seedlings and

the UV lamp in the experimental group. In order to avoid the influence of PVA film, a blank PVA film was placed between the control group and the UV light. After the exposure period, representative seedlings from both the experimental and control groups were sampled for growth evaluation. The fresh weight and length of each seedling were measured immediately. Subsequently, the samples were placed in a drying oven at 60 °C until a constant weight was achieved, and the dry weight was recorded. Finally, the β-carotene content of the pea seedlings was measured by means of an enzyme-linked immunosorbent assay (ELISA).

2.5. Characterization

Morphology studies were performed using scanning electron microscopy (SEM; ZEISS GeminiSEM 300, Carl Zeiss AG, Germany). The crystal structures of the samples were characterized using X-ray diffraction (XRD; Ultima IV, Rigaku Corporation, Japan). The *in-situ* XRD was measured at a heating rate of 10 K·min^{-1}, with measurements taken every 20 K. Rietveld structural refinement was performed using the Generalized Structure Analysis System (GSAS) program. Fourier-transform infrared (FTIR) spectroscopy (Spectrum GX FT-IR, PerkinElmer, Inc., USA) was performed at wavenumbers of 4000–400 cm^{-1}. The fluorescence spectra of the phosphors and phosphor films were measured using a spectrophotometer (FS5, Edinburgh Instruments Ltd., UK) at an excitation wavelength of 365 nm. X-ray photoelectron spectroscopy (XPS) analysis was observed on an ESCALAB 250 (Thermo Fisher Scientific, Inc., USA). Thermogravimetric analysis (TGA; TGA Q50, TA Instruments, USA) was performed from 313 to 1273 K. To determine the photoluminescence (PL) and photoluminescence excitation (PLE), the phosphor was excited at a low temperature using an optical parametric oscillator laser (NT342B-20-SH/SF, EKSPLA, Lithuania), and the emission spectrum were recorded with a charge-coupled device (CCD) detector (Glacier X, B&W Tek Inc., Japan). Specifically, PL spectra were collected under excitation from 250 to 595 nm with a step size of 1 nm, and the PLE curve was obtained by integrating the emission intensity of each PL spectrum. Based on the equipment, the temperature-dependent PL was measured by heating the phosphor from 5 to 310 K at a rate of 10 K·min^{-1}. Thermoluminescence (TL) glow curve spectra were recorded using a custom-made measurement system. The sample was initially cooled to 85 K and then stimulated by the excitation sources for 5 min. The sample was then heated to 700 K at a heating rate of 10 K·min^{-1}, and the emission intensity was recorded in real time. High-resolution VUV spectroscopy of YAG:Mn^{4+}–Mg^{2+} was conducted at 10 K using the beamline BL3B at the Ultraviolet Synchrotron Orbital Radiation (UVSOR) Facility (IMS Program, 24IMS6020, Institute for Molecular Science, Japan). Raman spectra were recorded using a LabRAM HR Evolution spectrometer (Horiba, Ltd., Japan) with a 785 nm near-infrared excitation laser.

3. Results and discussion

The phase-formation process of YAG during the calcination of the dried gel was characterized by *in-situ* XRD (Fig. 1(a)). Due to the use of a corundum sample holder, strong peaks matching the reference pattern of Al_2O_3 (the Joint Committee on Powder Diffraction Standards (JCPDS) card No. 02-1227) were present in the background. The characteristic peaks of $Y_3Al_5O_{12}$ (JCPDS card No. 33-0040) began to appear at 1103 K and became stronger as the temperature increased, which is consistent with the conclusion that sol–gel methods can lower the phase-formation temperature. Additionally, TGA revealed a significant weight loss in the calcining process, which resulted from the volatilization and decomposition of crystallization water and organic components in the gel (Fig. 1(b)). This also explains why the corundum peaks in the *in-situ* XRD patterns intensified with increasing temperature, as the shrinkage of the powder volume may have led to increased detection of the sample holder. Based on the TGA curve, we selected several representative temperature points and performed FTIR on the corresponding products (Fig. 1(c)). The untreated sample exhibited prominent absorption bands in the range of 3700–3000 cm^{-1}, indicative of hydroxyl (OH) groups, and in the range of 1500–1300 cm^{-1} suggesting the presence of carbonate (CO_3^{2-}) species, which were attributed to water and citric acid. As the temperature increased to 593 K, the intensity of the OH stretching vibrations decreased significantly, indicating a partial removal of adsorbed water. At 773 K, the carbonate peaks further diminished, and new absorption features emerged in the 1000–800 cm^{-1} region. As the temperature reached 1273 K, the FTIR bands became more distinct, indicating the appearance of crystal [36]. In fact, crystallization at higher temperatures above 1103 K was observed from the *in-situ* XRD. The results further confirmed that the heating process involved the evaporation of crystallization water, the decomposition of organic components, and the phase formation of YAG.

As shown in the Tanabe–Sugano diagram in Fig. 2(a), the free-ion terms of Mn^{4+} are ^4F, ^4P, and ^4G, where ^4F is the ground term, ^4P is an excited term, and ^4G is a higher-energy excited term. The Mn^{4+} ions can be strongly excited from the $^4A_2$ ground state derived from ^4F to the $^4T_1$ and $^4T_2$ excited states respectively originating from ^4F and ^4G via spin-allowed transitions; they then produce $^2E \rightarrow {}^4A_2$ red luminescence in the strong crystal field. Here, the term symbols such as $^4A_2$, ^2E, $^4T_1$, and $^4T_2$ denote the crystal filed electronic states of Mn^{4+} in octahedral coordination. The letters A, E, and T represent singly, doubly, and triply degenerate states, respectively. The superscript numbers indicate the spin multiplicity ($2S+1$, where S is the total spin quantum number). The subscript numbers distinguish different irreducible representations with the same degeneracy under crystal-field symmetry. The Mn^{4+} ions in the YAG host occupy the aluminum (Al) octahedral sites because the ionic radius of Mn^{4+} (0.53 Å) is similar to that of the Al^{3+} (0.535 Å) in its octahedral geometry (CN = 6). The PL and PLE spectra of YAG:Mn^{4+} at room temperature are shown in Fig. 2(b), which shows that the phosphors exhibit several broad excitation bands in the range of 250–550 nm when monitored at the emission wavelength (λ_{em}) of 672 nm and a narrow red luminescence peak at 672 nm under 320 nm excitation wavelength (λ_{ex}). The luminescence data were processed with International Commission on Illumination (CIE) 1931 to obtain chromaticity coordinates of (0.714, 0.286) for phosphor excited by UV light at 365 nm (Fig. S1 in Appendix A). The color purity of the YAG:Mn^{4+}–Mg^{2+} was calculated using the following equation [22]:

$$\text{Color purity} = \frac{\sqrt{(x-x_i)^2+(y-y_i)^2}}{\sqrt{(x_d-x_i)^2+(y_d-y_i)^2}} \times 100\% \quad (1)$$

where (x, y) represents the CIE chromaticity coordinates of the phosphor; (x_d, y_d) represents the CIE chromaticity coordinates of the dominant wavelength point (672 nm); and (x_i, y_i) represents the CIE chromaticity coordinates of standard white light (0.333, 0.333). The color purity of this phosphor is 94.96%, indicating excellent color quality.

Since Al^{3+} and Mn^{4+} have different valence states, some manganese ions may be stabilized as Mn^{3+} ions, which act as quenching centers to weaken the luminescence intensity of the phosphor, as shown in Fig. 2(c). Low-valence-state dopants can act as a charge compensator for Mn^{4+} in YAG, increasing the luminescence intensity [32]. In this work, we choose divalent cations (M^{2+}, where M = Mg, Zn, Ca, or Ba) with different ionic radii—as listed in Table S1 in Appendix A—as charge compensators to exclude the

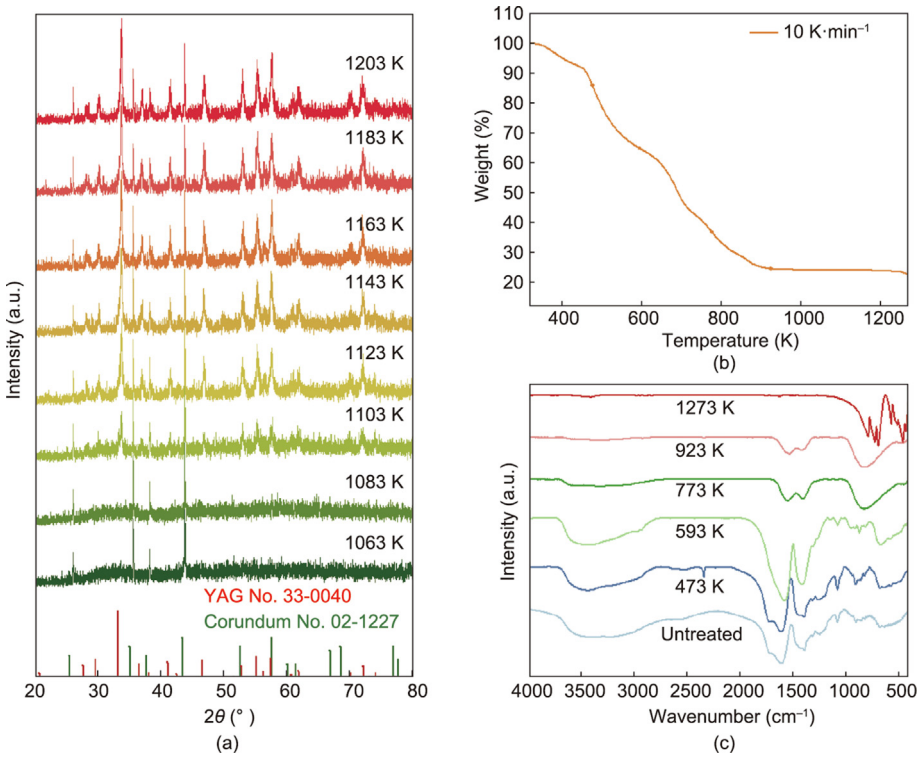

Fig. 1. (a) *In-situ* XRD analysis tests during calcination; (b) TGA curve of the precursor, at a heating rate of 10 K•min^{-1}; (c) FTIR of products obtained at different temperatures.

influence of valence states and explore the influence of doping sites on the luminescence properties. In the YAG host, there are two doping-site possibilities for M^{2+}: those of the 6-coordination Al^{3+} (CN = 6) or the 8-coordination Y^{3+} (CN = 8), determined by the ionic radii of M^{2+}. In both cases, a Mn^{4+} ion in an octahedral Al site ($Mn_{Al}^{\cdot}$) can be charge-compensated like M_Y' and M_{Al}'. The phosphors with different charge compensators matched well with the pure YAG phase (JCPDS card No. 33-0040), as shown in Fig. 2(d). Thus, the co-dopant ions were also substituted into the YAG crystal. To further distinguish between these different doped materials, the Raman spectra of the samples were characterized (Fig. S2 in Appendix A). For the strong red emission at 672 nm from Mn^{4+}, a wavelength of 785 nm in the near-infrared range was chosen to obtain the Raman spectrum. The obtained Raman spectrum can be divided into three frequency regions: the low-frequency region (<500 cm^{-1}), the intermediate region (500–600 cm^{-1}), and the high-frequency region (600–900 cm^{-1}). The YAG:Mn^{4+}–Ba^{2+} sample exhibited peaks that differed from the typical YAG Raman spectra; this might be due to the significant difference in ionic radii between the Ba^{2+} and the doping sites, which made it impossible for the Ba ions to smoothly replace the original ions. As the ionic radius of the charge compensator decreased, the Raman peaks became progressively sharper, suggesting an enhancement in structural symmetry and crystallinity. Among all the samples, the sample co-doped with Mg^{2+} displayed the sharpest and most well-defined Raman features, indicating that Mg^{2+} was the most effective ion for doping the site. Fig. 2(e) shows the diffuse reflection spectra of undoped and M^{2+}-doped YAG:Mn^{4+} samples, respectively. All samples with a charge compensator show a strong drop in the reflection spectrum in the UV range at around 334 nm, corresponding to the charge transfer (CT) band between O^{2-} and Mn^{4+}. For YAG:Mn^{4+}, a UV absorption band is observed at around 280 nm, which is different from the UV absorption band of the co-doped samples. In addition, there is no absorption band in the visible range. For the YAG:Mn^{4+}–M^{2+} samples, an additional absorption band is observed at 500 nm, which can be attributed to the $^4A_2 \rightarrow {}^4T_1$ transition of the Mn^{4+} ions [37]. These results show that the presence of a charge compensator increases the content of tetravalent manganese ions in YAG; almost all the manganese ions in the YAG:Mn^{4+} sample change into Mn^{3+}, and the UV band at 280 nm of YAG:Mn^{4+} is likely due to the CT between O^{2-} and Mn^{3+}.

Here, we would like to discuss the site occupancy of the charge compensators. Considering a 30% tolerance of the ionic radii of Al^{3+} (CN = 6) and Y^{3+} (CN = 8), the YAG host can accept ions with an ionic radius of 0.375–0.696 Å in Al sites and an ionic radius of 0.713–1.330 Å in yttrium (Y) sites. Thus, almost all the divalent co-dopants—except for Ba^{2+}—can occupy the dodecahedral Y site, but this is not the case for the octahedral Al site. However, it is known that $\{NaCa_2\}[Mg_2](V_3)O_{12}$ and $\{NaCa_2\}[Zn_2](V_3)O_{12}$ have a garnet structure [38]. It should be noted that these materials with garnet structures have much larger lattice constants than YAG, which affects their tolerance for the ionic radius of doping ions. The substitution of Ca^{2+} to an octahedral site within a garnet structure is very rare, but substitution does occur with Ba^{2+}. Thus, a small amount of Mg^{2+} and Zn^{2+} ions may occupy octahedral sites even in the YAG host. However, it is also known that, while $\{Ca_3\}[Sc_2](Si_3)O_{12}$ [39] and $\{Y_2Mg\}[Mg_2](Ge_3)O_{12}$ [40] garnet structures exist, dodecahedral barium (Ba) garnets and dodecahedral zinc (Zn) garnets have never been reported. Based on this fact, it appears that Ca^{2+} and Zn^{2+} ions can be substituted into the dodecahedral Y site and the octahedral Al site, respectively. Mg^{2+} ions have two possible substitution sites—the dodecahedral site and the octahedral site. Ba ions are only able to occupy dodecahedral sites due to their large ionic radius.

To further identify the crystallographic site occupation of the charge compensation in the YAG host, Rietveld structural refinement was performed with two conditions (dodecahedral-site and octahedral-site occupations) using the GSAS program, as shown in Figs. S3(a)–(d) in Appendix A [41]. Based on the smaller residual

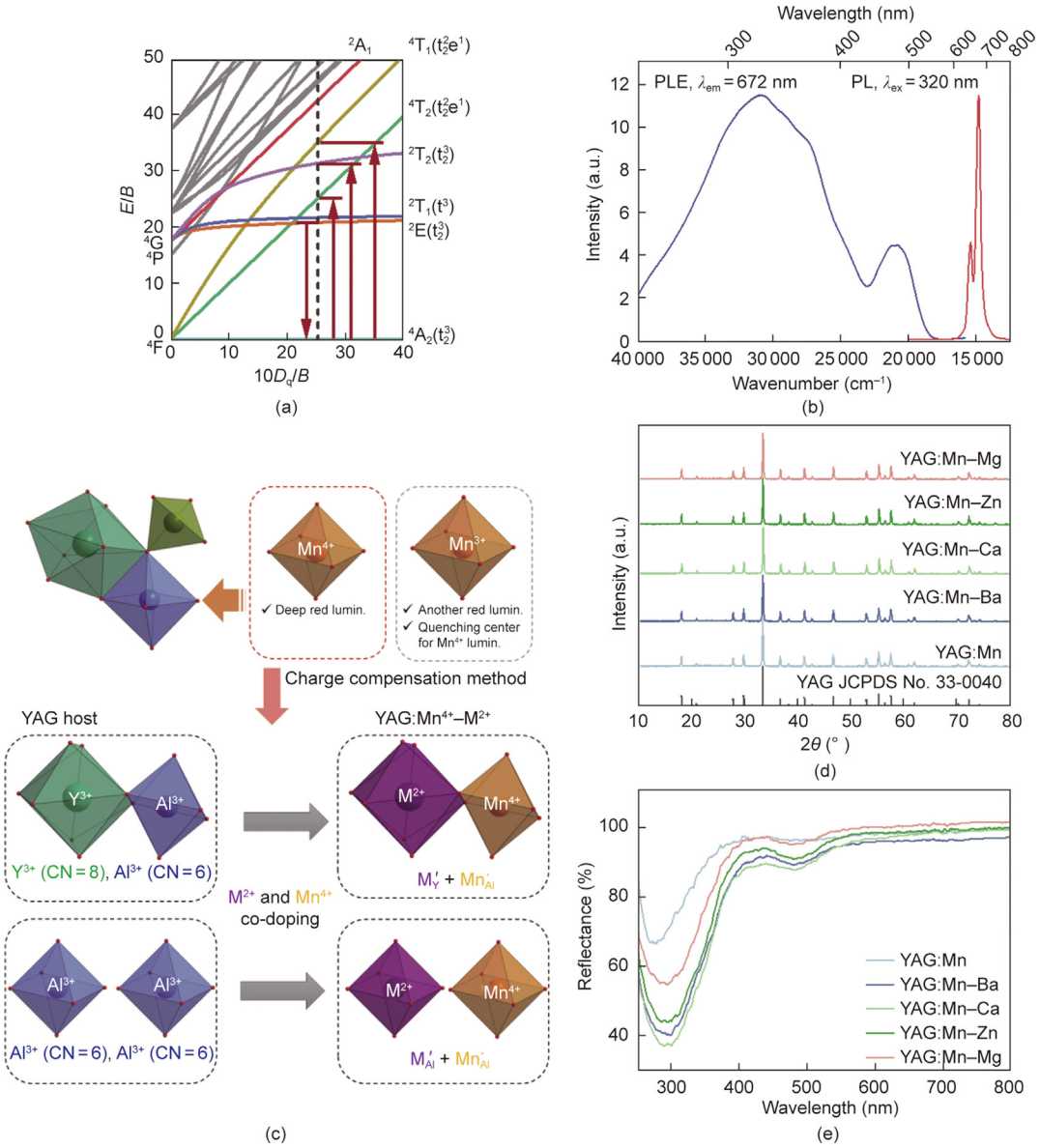

Fig. 2. (a) Tanabe–Sugano diagram of a Mn^{4+} ion in an octahedron geometry (*E*: the energy of the corresponding crystal-field state; *B*: Racah parameter; D_q: the crystal field splitting parameter); (b) PLE and PL spectra at room temperature; (c) schematic diagram of charge compensation (lumin.: luminescence). (d) XRD pattern and (e) diffuse reflection spectra of YAG:0.2%Mn^{4+}–4%M^{2+}(simplified as YAG:Mn–M in figures; the same applies to the following figures).

factors of profile factor (R_p), weighted profile factor (R_{wp}), and goodness-of-fit statistic (χ^2), it was found that Zn and magnesium (Mg) prefer to occupy octahedral sites, while calcium (Ca) and Ba prefer to occupy dodecahedral sites. Table S2 in Appendix A shows the cell parameters, 6-coordination Al–O bond lengths, and 8-coordination Y–O bond lengths with suitable site occupation of the charge compensators. Compared with pure YAG ($a = 12.00$ Å), all the obtained samples doped with Mn^{4+}, which has a larger ionic radius than Al^{3+} (CN = 6), and with M^{2+} at the corresponding substitutional sites exhibit a larger lattice constant. The large lattice constants and the convincing residual factors ($R_p < 10\%$, $R_{wp} < 15\%$, $\chi^2 < 2$) of the Rietveld refinement indicate that the charge compensator can be doped into the YAG host.

Fig. 3(a) shows the PL spectra of YAG:Mn^{4+} with various charge compensators. The luminescent intensity of the Mn^{4+}:^2E–$^4A_2$ transition is enhanced by the M^{2+} co-doping in the following order: $Ba^{2+} < Ca^{2+} < Zn^{2+} < Mg^{2+}$. As the ionic radius of the charge compensator decreases, the luminescence intensity increases. These results indicate that the M^{2+} charge compensator to the octahedral site, rather than to the dodecahedral site, enhances the luminescent intensity due to Mn^{4+} stabilization (Figs. 3(a) and (b)). This is consistent with the PL intensity effectively being increased by Mg^{2+} co-doping, as reported in the literature [31].

Fig. 3(b) shows the luminescence decay curves of the Mn^{4+}:^2E–$^4A_2$ transition in YAG:Mn^{4+} with various charge compensators; the fitting process is described in Section S1 in Appendix A. The luminescence decay curves differ slightly among the different samples; they do not follow a single-order exponential function, indicating the presence of quenching processes. To evaluate the lifetime, the decay curves were mechanically fitted with a second-order exponential equation:

$$I(t) = A_1 e^{-\frac{t}{\tau_1}} + A_2 e^{-\frac{t}{\tau_2}} \quad (2)$$

where $I(t)$ is the luminescence intensity at time t, A_1 and A_2 are the initial intensities, and τ_1 and τ_2 indicate the corresponding life-

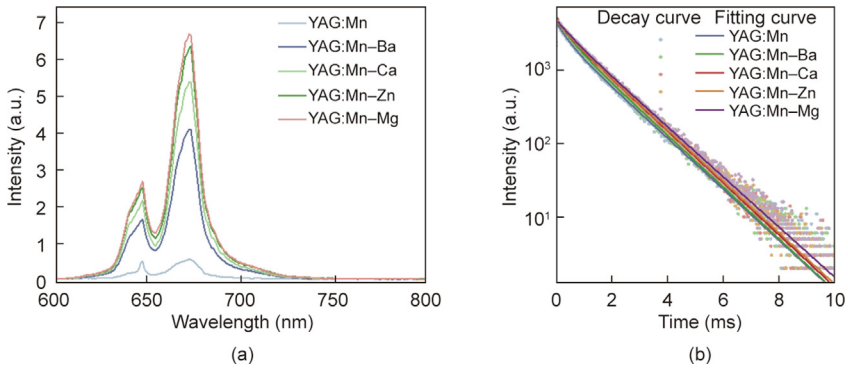

Fig. 3. (a) PL spectra; (b) decay curves and fitting curves of YAG:0.2%Mn^{4+}–4%M^{2+}.

times, respectively. The average lifetime (τ) can be calculated as follows:

$$\tau = \frac{A_1\tau_1^2 + A_2\tau_2^2}{A_1\tau_1 + A_2\tau_2} \quad (3)$$

The lifetimes of YAG:Mn^{4+}, YAG:Mn^{4+}–Ba^{2+}, YAG:Mn^{4+}–Ca^{2+}, YAG:Mn^{4+}–Zn^{2+}, and YAG:Mn^{4+}–Mg^{2+} were determined to be 1.103, 1.105, 1.150, 1.163, and 1.188 ms, respectively. The lifetime increases with a decrease in the ionic radius, which is consistent with the trend of PL intensity. This is probably because the Mn^{3+} quenching center is reduced by the charge compensator.

The structure of the YAG:Mn^{4+}–Mg^{2+} sample was characterized, and the results are shown in Fig. 4. The XPS spectrum was presented in Fig. 4(a). In addition to the strong signals of the Y, Al, and O, the Mg signal can be observed at 1299 eV and is ascribed to the binding energy of Mg 1s (Fig. S4 in Appendix A). However, the Mn^{4+} content is too small to be detected. A comparison indicates that the ratio of the Y, Al, Mg, and O elements obtained by means of XPS is basically the same as the theoretical ratio, as shown in Table S3 in Appendix A. In addition, the corresponding atomic ratio of Y:Al:Mn:Mg, as measured by energy-dispersive X-ray spectroscopy (EDS) (Fig. 4(d)), was determined to be 40.09:58.99:0.02:0.90, which is generally consistent with the theoretical value.

The valence state of the Mn ion was investigated using X-ray absorption near edge structure (XANES) spectra, as shown in Fig. 4(b). In the figure, the absorption edge of the YAG:Mn^{4+} single-doped sample is located between those of the reference samples Mn_2O_3 and MnO, in line with Fig. 2(c), indicating that the Mn is more likely to exhibit a trivalent state when doped into the Al site. After co-doping with Mg^{2+}, the curve moved to the right, to a position closer to MnO_2, indicating that the addition of

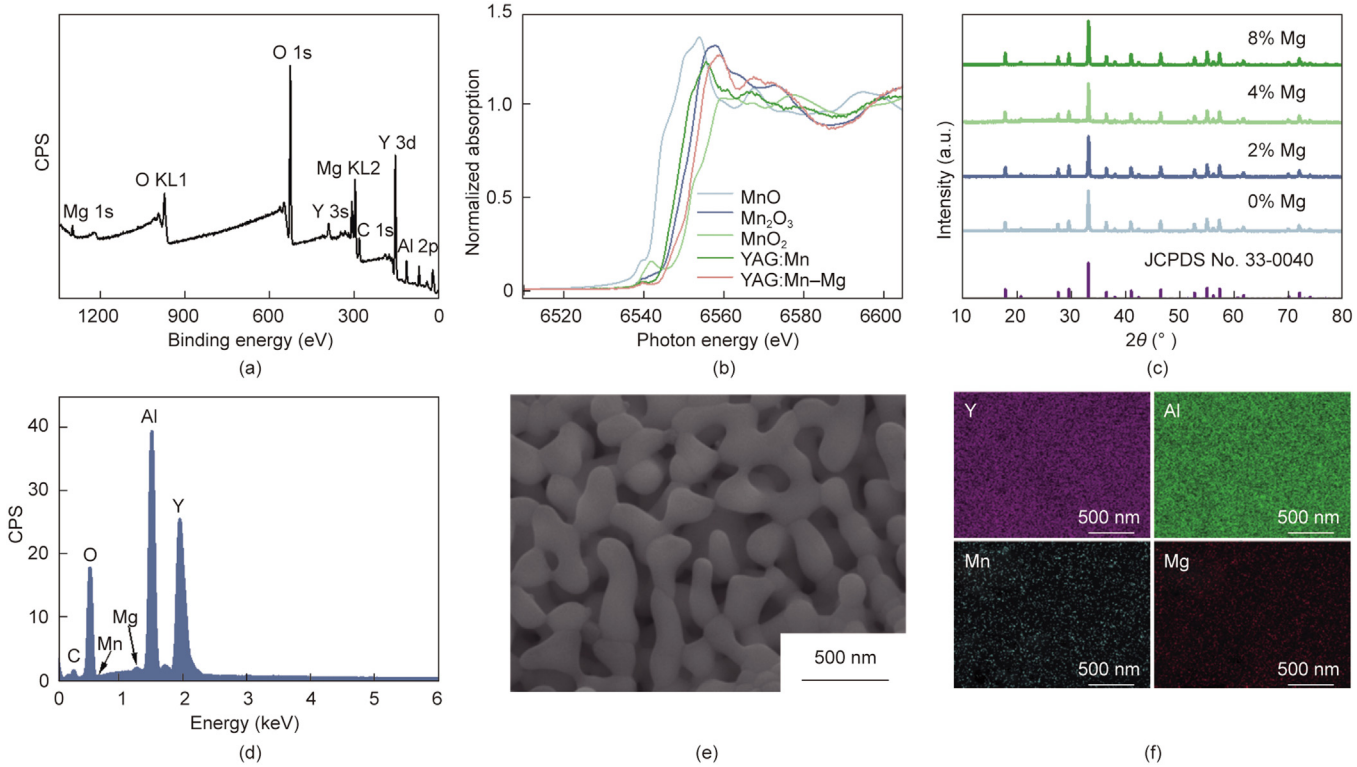

Fig. 4. (a) XPS survey spectrum (CPS: counts per second); (b) X-ray absorption near edge structure (XANES) spectra and a series reference compounds, Mn_2O_3, MnO_2, and MnO; (c) XRD pattern. (d) EDS spectrum, (e) SEM image, and (f) false-color elemental mapping of the Y (purple), Al (green), Mn (blue), and Mg (red) of YAG:0.2%Mn^{4+}–4%Mg^{2+}.

the charge compensator increased the content of tetravalent manganese ions. Although the ratio of Mn^{4+} to Mn^{3+} definitely increased, based on the reflectance spectrum and PL spectra, the XANES result indicates that there are still many Mn^{3+} ions in the YAG host. If all the Mn^{3+} ions can be oxidized into Mn^{4+}, it is expected that the YAG:Mn^{4+} will exhibit a much stronger red luminescence. The morphology and microstructure of the sintered samples at 1200 °C were characterized by means of SEM. As shown in Figs. 4(e) and (f), the metal elements are evenly distributed across every particle, as the sol–gel method can achieve uniform mixing of cations at the atomic level.

Using the most intense YAG:Mn^{4+}–Mg^{2+} sample, the luminescence properties of the Mn^{4+} ions in the YAG matrix were further investigated. To show that the phosphor crystals were of high quality, TL glow curves of YAG:Mn^{4+}–Mg^{2+} after illumination by a UV light source were recorded (Fig. 5(a)). No obvious peak below 600 K was observed, which implies that there are almost no crystalline defects to trap carriers, and the Mg co-dopant acts as a correct charge compensator. Fig. 5(b) shows the PLE spectrum of the red luminescence of YAG:Mn^{4+}–Mg^{2+} on an energy scale. In the $3d^3$ electron configuration, spin-allowed transitions due to $^4A_2 \rightarrow {}^4T_2$ and $^4T_1$ are generally located in the UV to visible range. Unlike typical Mn^{4+}-doped fluoride phosphors, there is a very broad PLE band in YAG:Mn^{4+} around the second band of $^4A_2 \rightarrow {}^4T_1$ in the range from 250 to 450 nm (Fig. 5(b)). In oxide host materials, a CT band corresponding to the transition from the O^{2-}–Mn^{4+} to the O^-–(Mn^{4+}–e^-) overlaps with $^4T_1$ band. Therefore, the PLE bands were fitted by three Gaussian bands, and the centroid energies of the CT, $^4A_2 \rightarrow {}^4T_1$, and $^4A_2 \rightarrow {}^4T_2$ were estimated to be 31 053, 27 164, and 20 794 cm^{-1}, respectively. To further explain the effect of the crystal field intensity on the red emission of YAG:Mn^{4+}, the $^4A_2$ ground state is regarded as 0 eV, and the crystal field splitting parameter (D_q) and Racah parameters (B and C) can be calculated using Eqs. (4)–(6), according to the zero phonon line (ZPL) for ^2E and the centroid energy for $^4T_{1,2}$ [22,42]:

$$E(^4T_2)_{ZPL} = 10D_q \tag{4}$$

$$\frac{B}{D_q} = \frac{(\Delta E/D_q)^2 - 10(\Delta E/D_q)}{15(\Delta E/D_q - 8)} \tag{5}$$

$$\frac{E(^2E)_{ZPL}}{B} = \frac{3.05C}{B} + 7.90 - \frac{1.80B}{D_q} \tag{6}$$

where E represent the energy of the corresponding crystal-field state, which is obtained from the spectral peak position of the related transition. $\Delta E = E(^4T_1)_{ZPL} - E(^4T_2)_{ZPL}$. For the convenience of calculation, the energy corresponding to the peak of the $^4A_2 \rightarrow {}^4T_2$ transition is regarded as $E(^4T_2)$, and the energy difference between the peaks of the two transition bands $^4A_2 \rightarrow {}^4T_1$ and $^4A_2 \rightarrow {}^4T_2$ is regarded as ΔE.

However, for Mn^{4+}-doped oxide phosphors, it is more challenging to accurately determine the $E(^4T_1)_{ZPL}$ due to the complexity of the excitation spectra. In addition, considering only the exactly determinable $E(^2E)_{ZPL}$ and $E(^4T_2)_{ZPL}$ parameters from experiments, we assume that $C/B = 4.7$; B, C, and $E(^4T_1)_{ZPL}$ can be obtained from standard crystal-field theory, as follows [43]:

$$B = 6.18D_q - \frac{1}{2}\left[12.36(D_q)^2 - 2.22E(^2E_g)D_q\right]^{1/2} \tag{7}$$

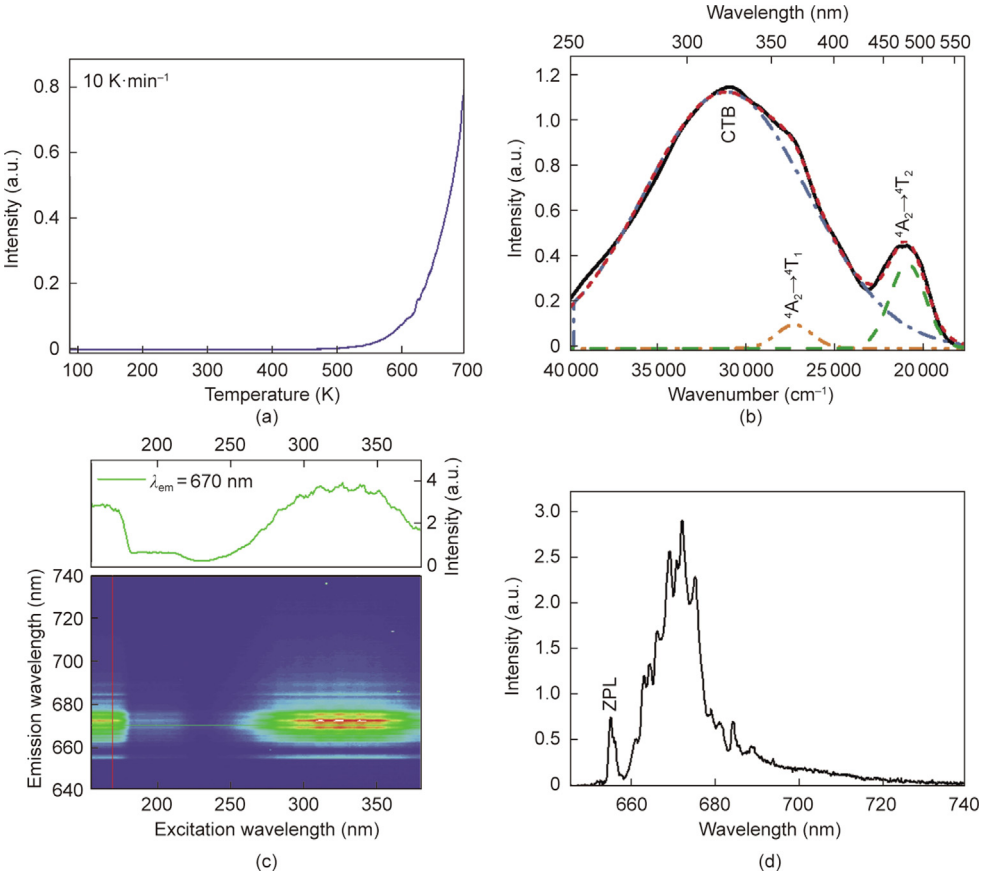

Fig. 5. (a) TL glow curve of YAG:Mn^{4+}–Mg^{2+} with a heating rate of 10 K·min^{-1}; (b) PLE spectrum (λ_{em} = 672 nm; CTB: charge transfer band); (c) 2D contour plot of PL intensity excitation–emission wavelength at 10 K; (d) emission spectra corresponding to (c) (λ_{ex} = 316 nm).

$$C = 4.7B \tag{8}$$

$$E\left({}^4T_1\right)_{ZPL} = 7.5B + 15D_q - \frac{D_q}{2}\left[\left(\frac{15B}{D_q} + 10\right)^2 - \frac{480B}{D_q}\right]^{1/2} \tag{9}$$

The values of D_q, B, and C were respectively calculated to be 2079.40, 823.25, and 3869.28 cm^{-1}, and the value of $10D_q/B$ is 25.26, which is >22, indicating that the Mn^{4+} ions are in a strong crystal field. The Tanabe–Sugano diagram of a Mn^{4+} ion in an octahedron geometry is provided in Fig. 2(a).

Fig. S5 in Appendix A shows the PLE and PL of YAG:Mn^{4+}–Mg^{2+} at a low temperature. At 5 K, the PLE spectra above 250 nm was almost the same as that at room temperature. However, scanning the excitation wavelength below 250 nm revealed two additional PLE bands at 190 and 175 nm (Fig. 5(c)). The PLE band at 175 nm (~7.09 eV) can be identified as the host exciton peak (E^{ex}) because of previous reports of the host exciton energy of YAG [44], but the PLE band at 190 nm is unclear. Considering a binding energy of $0.008 \times (E^{ex})^2$, the band gap was estimated to be 7.49 eV. From the density functional theory (DFT) calculation, both the valence band (VB) top and the conduction band (CB) bottom are created at the Γ point (Fig. S6(a) in Appendix A). Thus, the band-to-band absorption is attributed to the direct bandgap. From the projected density of states (PDOS), the VB is formed mainly by the O 2p, and the CB by the Y 4d (Fig. S6(b) in Appendix A).

As shown in Fig. 5(d), a sharp PL peak was observed at 655 nm—the shortest wavelength of several PL peaks. Since the thermal excitation to the higher phonon levels of the excited state can be ignored at 5 K, the sharp peak can be attributed to the ZPL of the Mn^{4+} $^2E \rightarrow {}^4A_2$ transition. Several peaks above 655 nm can be attributed to the Stokes phonon side bands (PSBs). Moreover, only one type of ZPL at 655 nm was observed from any excitation from UV to visible range (Fig. 5(d)), indicating that there is only one Mn^{4+} luminescence center. The energies of the Stokes PSBs were analyzed and are listed in Appendix A (Section S3, Fig. S7, and Table S4) [42].

In order to further investigate the PL properties, the temperature–emission (T–λ) 2D contour mapping was obtained (Figs. 6(a) and (b)). As the temperature increases, the Stokes PSBs at around 672 nm and the ZPL show a downward trend (Fig. 6(c)). In addition, the ZPL shifts to lower energy. This is a typical ZPL energy shift, mainly caused by the two-phonon resonant Raman process. On the other hand, the PL band at 647 nm increases with increasing temperature, indicating that this is the anti-Stokes PSBs. The intensity ratio between the anti-Stokes and Stokes phonon sidebands is as follows [45]:

$$\frac{I_{AS}}{I_S} = ce^{-h\nu_{eff}/(k_B T)} \tag{10}$$

where I_{AS} and I_S are the integrated intensities of the anti-Stokes and Stokes emissions, respectively; c is a constant that accounts for the combined effects; $h\nu_{eff}$ is the effective phonon energy; k_B is the Boltzmann constant; and T is the absolute temperature. Fig. 6(d) presents the relationship between $\ln(I_{AS}/I_S)$ and the inverse temperature $1/T$ that is used to estimate $h\nu_{eff}$. From the Arrhenius plot, the effective phonon energy is calculated to be 319.31 cm^{-1}, which is similar to the phonon energy (311, 352, and 380 cm^{-1}) around the main peak of the PL spectrum in Fig. S7. This characteristic can be used for a luminescent thermometer, due to the significant change in the ratio of the anti-Stokes/Stokes emission intensity that occurs with temperature. Thus far, $LaAlO_3$:Mn^{4+} [46] and K_2TiF_6:Mn^{4+} [47] have been reported to be used as thermometers, utilizing the relationship between temperature and the intensity ratio of the anti-Stokes and Stokes emission lines. Senden et al. [48] reported the relationship between the quenching temperature $T_{1/2}$ and the ${}^4A_2 \rightarrow {}^4T_2$ transition energy and discussed the quench-

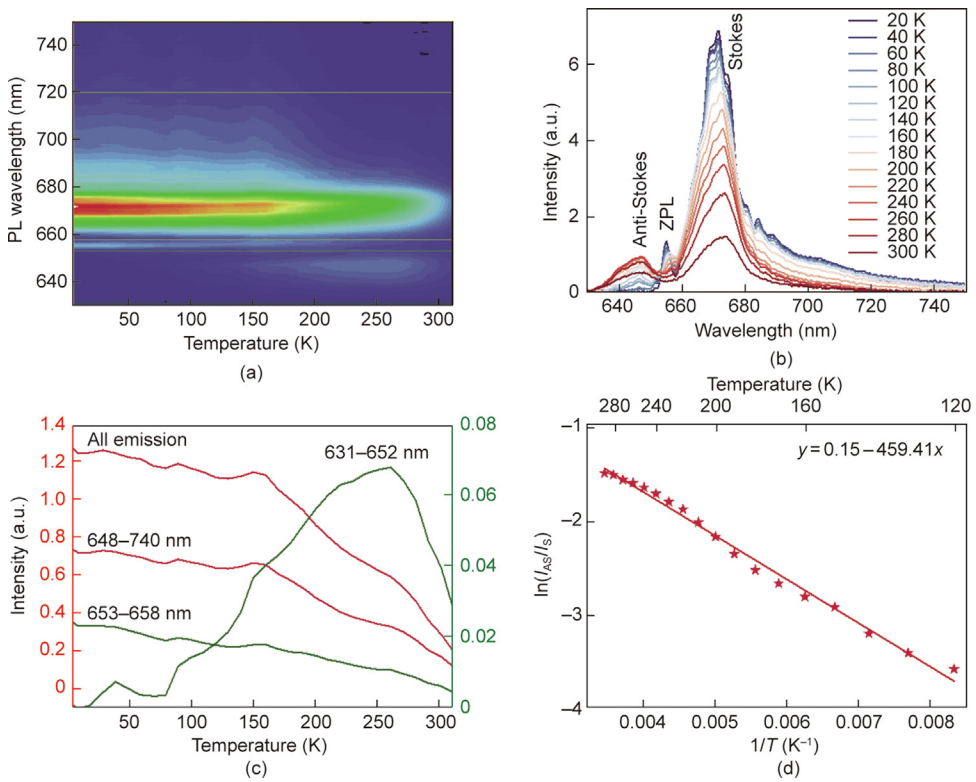

Fig. 6. (a) Temperature–emission (T–λ) 2D contour mapping; (b) temperature-dependent PL spectra of YAG:Mn^{4+}–Mg^{2+} excited at 480 nm; (c) temperature-dependent PL intensity at different wavelength regions; (d) temperature-dependent PL intensity ratio as a function of inverse temperature.

ing process; the researchers clearly showed that the quenching process of $^2E \rightarrow {}^4A_2$ luminescence is caused by a thermally activated crossover through the $^4T_2$ energy state [48]. As shown in Fig. 6(c), $T_{1/2}$ was 254 K. Thus, the newly-estimated quenching temperature of YAG:Mn^{4+}–Mg^{2+} was plotted into the $T_{1/2}$ versus $^4A_2 \rightarrow {}^4T_2$ transition energy graph, as shown in Fig. S8 in Appendix A. The result indicates that the emission of Mn^{4+} in the YAG host is similarly quenched due to a thermally activated crossover from the $^4T_2$ excited state to the $^4A_2$ ground state.

The optimal concentrations of Mn^{4+} and Mg^{2+} were also explored in this work. The following red phosphors were prepared: YAG:$m$$Mn^{4+}$–$n$$Mg^{2+}$ (m = 0.05%, 0.1%, 0.2%, and 0.3%; n = 0%, 2%, 4%, and 8%). The PL spectra and pictures are exhibited in Fig. S9 in Appendix A. With an increase in the Mn^{4+} concentration, the luminescence intensity showed a trend of first increasing and then decreasing, which was caused by concentration quenching. A comparison showed that the phosphor with the best luminescent properties was YAG:0.2%Mn^{4+}–4%Mg^{2+}.

For application purposes, the weatherproof properties of the phosphor were also studied. The luminescence intensity of the phosphor was tested by drying after the following treatments: soaking in pure water for 15 d, soaking in an aqueous hydrochloric acid (HCl) solution with a pH of 1.57 for 5 h, and soaking in an aqueous sodium hydroxide (NaOH) solution with a pH of 12.65 for 5 h. According to the results presented in Fig. 7(a), the phosphor continued to maintain strong luminescence after treatment under such extreme conditions. This resistance to moisture, acidity, and alkalinity makes the phosphor suitable for the special humid environment in which plant lighting would typically be used. In addition, in order to determine the optical properties of the phosphor at higher temperatures, the PL spectra of the YAG:Mn^{4+}–Mg^{2+} were measured above 300 K. As expected based on the temperature dependence below 300 K, the PL intensity decreased rapidly with an increase in temperature, which indicates low light-conversion efficiency from UV to red light at higher temperatures (Fig. 7(b)). However, this rapid decrease may provide an advantage: The temperature of the light-conversion film will increase more rapidly with higher sunlight intensity on clear days. It is known that intense sunlight can damage photosystems and decrease their photosynthetic output, thereby inhibiting plant growth and development [49]. Thus, this luminescence quenching can automatically avoid excess light illumination for plants.

PVA does not affect the luminescence of the phosphors (Figs. S10(a) and (b) in Appendix A); moreover, it has good mechanical properties and film formation. This material can also be degraded by microorganisms into CO_2 and H_2O, making it harmless to the environment and suitable for light-conversion films. The light-conversion film obtained by mixing PVA and the YAG:Mn^{4+}–Mg^{2+} phosphors can convert the portion of natural light that would normally be useless for plant growth into red light to promote plant growth without any other energy inputs, as shown in Fig. 8(a). Adding phosphor doping further improves the light-conversion performance (Fig. S10(c) in Appendix A); however, due to the poor compatibility of rare earth inorganic compounds with PVA, it can also lead to a decrease in the light transmittance. Therefore, a 6% doping concentration was considered most appropriate. The properties of the PVA and phosphors in the light-conversion film obtained via the physical blending method were not changed. The characteristic peaks of the YAG:Mn^{4+}–Mg^{2+} phosphors were still very obvious in the XRD pattern. In addition, a characteristic peak at 20° appeared, which was attributed to PVA. It also can be seen from the FTIR spectra of the films (Figs. S10(d) and (e) in Appendix A) that the chemical bonding in the PVA was not affected. As a result, the thermal decomposition of the film was basically unchanged and can be divided into three stages: the evaporation of water molecules, the start of the decomposition of functional groups, and the carbonization of the PVA film. The residual weight difference between the blank PVA film and the light-conversion film was 4.8%, which was basically consistent with the amount of phosphor added (Fig. S10(f) in Appendix A). As a proof of concept, a plant growth experiment was done, and an additional UV lamp was used to amplify the difference. As shown in Fig. 8(a), the pea seedlings were divided into two groups. Blank PVA film (group A, the control group) and light-conversion film (group B, the experimental group) were respectively placed between the pea seedlings and the UV lamp. Both groups were then cultivated under the same humidity and temperature conditions for 8 d. It can be seen from the comparison in Figs. 8(b)–(e) that the growth of group B was better than that of group A. The plant height, total length with root, and plant weight were measured. Compared with that of group A, the height in group B was 11.3% greater, the total length with root increased by 41.3%, the fresh weight increased by 39.0%, and the dry weight increased by 10.8%. Moreover, as red light can promote the synthesis and accumulation of β-carotene in the leaves of pea seedlings, the β-carotene content in the pea seedlings increased by 14.22% after red light treatment.

4. Conclusions

In this work, the red phosphor YAG:Mn^{4+} was prepared, and its luminescence properties were optimized via charge compensation. It was observed that the phosphor's emission intensity was significantly improved by co-doping with Mg^{2+}. More detailed PL characteristics were revealed in the PL spectrum obtained at a low temperature, and it was determined that the position of the ZPL was at 655 nm. With increasing temperature, anti-Stokes PSBs appeared below 655 nm. The effective phonon energy was estimated based on the temperature dependence of the luminescence

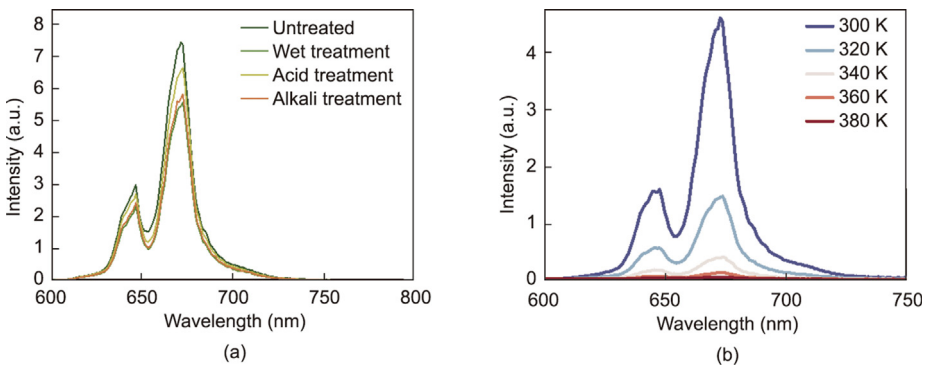

Fig. 7. (a) PL spectra of the phosphors after various extreme treatments; (b) PL spectra of the phosphors at different temperatures.

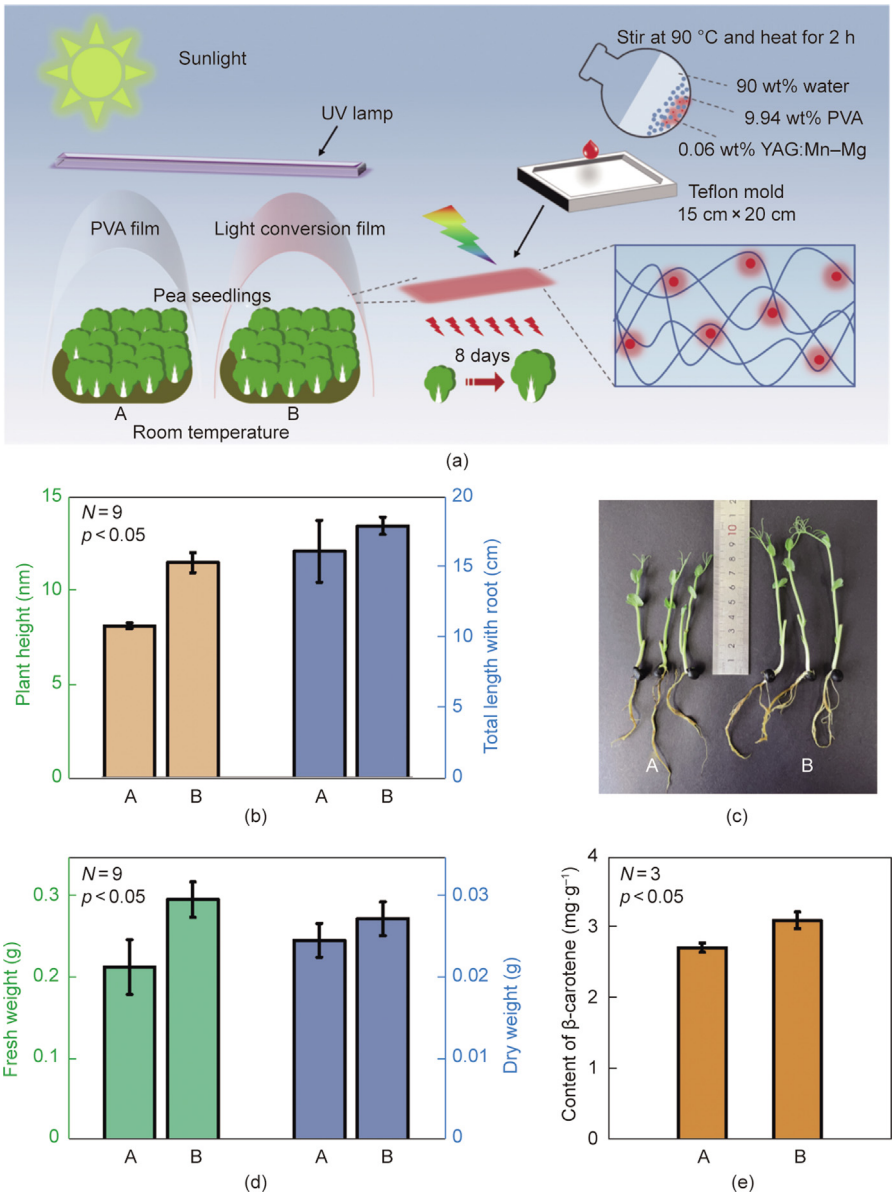

Fig. 8. (a) Schematic diagram of the light-conversion film working. (b–e) Comparison of the (b) plant height and total length with root, (c) picture of pea seedlings, (d) weight, and (e) β-carotene content of group A vs group B.

intensity ratio of the anti-Stokes PSBs to the Stokes PSBs, which can be used as an optical thermometer. The phosphor exhibited temperature quenching at high temperatures due to a thermally activated crossover from the $^4T_2$ excited state to the $^4A_2$ ground state. With its broad excitation band, deep red light emission, and resistance to moisture, acidity, and alkalinity, this phosphor shows strong potential for plant lighting applications. In a plant cultivation experiment, pea seedlings grown under a red light-conversion film prepared with this phosphor exhibited greater length, heavier weight, and higher β-carotene content than those grown with blank PVA film. This result demonstrates that the phosphor presented herein has potential for use in agricultural lighting applications.

CRediT authorship contribution statement

Fen Wang: Writing – original draft, Methodology, Investigation, Data curation. **Hirohisa Miyata:** Writing – review & editing, Methodology, Investigation. **Jingyi Liang:** Writing – review & editing, Methodology, Investigation. **Yingying Song:** Writing – review & editing, Methodology, Investigation. **Guangyuan Xu:** Writing – review & editing, Methodology, Investigation. **Jumpei Ueda:** Writing – review & editing, Supervision, Resources, Project administration, Methodology, Investigation, Conceptualization. **Dan Wang:** Writing – review & editing, Supervision, Resources, Project administration, Methodology, Funding acquisition, Conceptualization.

Declaration of competing interest

The authors declare that they have no known competing financial interests or personal relationships that could have appeared to influence the work reported in this paper.

Acknowledgments

This work was supported by the National Natural Science Foundation of China (22278027), the Japan Society for the Promotion of

Science (JSPS) KAKENHI (24K01581), and the Joint Studies Program of the Institute for Molecular Science (24IMS6020). The XANES measurements were performed under the approval of the Photon Factory Program Advisory Committee (2024G629). Fen Wang acknowledges the China Scholarship Council (CSC 202406880037) for supporting her during a visit of Japan Advanced Institute of Science and Technology (JAIST).

Appendix A. Supplementary data

Some of the information from this work, including descriptions of lifetime fitting, Raman spectra, DFT calculations, a detailed PL analysis, the crystal structure and crystallographic parameters, pictures of phosphors, and the characterization of films is presented in the supplementary material. Supplementary data to this article can be found online at https://doi.org/10.1016/j.eng.2025.09.035.

References

[1] Kuang T. A breakthrough of artificial photosynthesis. Natl Sci Rev 2016;3(1):2–3.
[2] Dogutan DK, Nocera DG. Artificial photosynthesis at efficiencies greatly exceeding that of natural photosynthesis. Acc Chem Res 2019;52(11):3143–8.
[3] Florez-Velasco N, Ramos VF, Magnitskiy S, Balaguera-López H. Ethylene and jasmonate as stimulants of latex yield in rubber trees (*Hevea brasiliensis*): molecular and physiological mechanisms. A systematic approximation review. Adv Agrochem 2024;3(4):279–88.
[4] Tong X, Tang J, Wang J, Wu Y, Zheng Z, Yuan C, et al. Engineered biodegradable nanopesticides for efficient leaf deposition and plant fungicides. AIChE J 2024;70(6):e18414.
[5] Yin X, Li Y. Plants self-synthesize "agrochemical" to fight pests and diseases. Adv Agrochem 2025;4(1):5–7.
[6] Dakora FD, Li H, Zhao J. Exploring the impacts of elevated CO_2 on food security: nutrient assimilation, plant growth, and crop quality. Engineering 2025;44:234–44.
[7] Wang P, Abid MA, Qanmber G, Askari M, Zhou L, Song Y, et al. Photomorphogenesis in plants: the central role of phytochrome interacting factors (PIFs). Environ Exp Bot 2022;194:104704.
[8] Meng L, Zhou Y, Román MO, Stokes EC, Wang Z, Asrar GR, et al. Artificial light at night: an underappreciated effect on phenology of deciduous woody plants. PNAS Nexus 2022;1(2):pgac046.
[9] Li Z, Chen Q, Xin Y, Mei Z, Gao A, Liu W, et al. Analyses of the photosynthetic characteristics, chloroplast ultrastructure, and transcriptome of apple (*Malus domestica*) grown under red and blue lights. BMC Plant Biol 2021;21(1):483.
[10] Chen X, Cai W, Xia J, Yu H, Wang Q, Pang F, et al. Metabolomic and transcriptomic analyses reveal that blue light promotes chlorogenic acid synthesis in strawberry. J Agric Food Chem 2020;68(44):12485–92.
[11] Huang X, Hu L, Kong W, Yang C, Xi W. Red light-transmittance bagging promotes carotenoid accumulation of grapefruit during ripening. Commun Biol 2022;5(1):303.
[12] Rouached H. Red light means on for phosphorus. Nat Plants 2018;4(12):983–4.
[13] Midorikawa K, Tateishi A, Toyooka K, Sato M, Imai T, Kodama Y, et al. Three-dimensional nanoscale analysis of light-dependent organelle changes in *Arabidopsis* mesophyll cells. PNAS Nexus 2022;1(5):pgac225.
[14] SharathKumar M, Heuvelink E, Marcelis LFM, Van Ieperen W. Floral induction in the short-day plant chrysanthemum under blue and red extended long-days. Front Plant Sci 2021;11:610041.
[15] Zhang S, Chen Z, Cao C, Cui Y, Gao Y. Photothermal-management agricultural films toward industrial planting: opportunities and challenges. Engineering 2024;35:191–200.
[16] Lauria G, Lo Piccolo E, Ceccanti C, Guidi L, Bernardi R, Araniti F, et al. Supplemental red LED light promotes plant productivity, "photomodulates" fruit quality and increases *Botrytis cinerea* tolerance in strawberry. Postharvest Biol Technol 2023;198:112253.
[17] Wu C, Wang W, Zhu K, Li W, Cai D, Chen Z, et al. An efficient and universal solar interfacial photothermal reactor toward liquid phase oxidation. AIChE J 2023;69(5):e17995.
[18] Hong C, Zhong R, Xu M, He P, Mo H, Qin Y, et al. Interactions among food systems, climate change, and air pollution: a review. Engineering 2025;44:215–33.
[19] Chu X, Zhang P, Shi S, Liu Y, Feng W, Zhou N, et al. Hydrophobic self-cleaning micro-nano composite polyethylene-based agricultural plastic film with light conversion and abrasion resistance. Colloids Surf A 2023;658:130621.
[20] Liu Y, Gui Z, Liu J. Research progress of light wavelength conversion materials and their applications in functional agricultural films. Polymers 2022;14(5):851.
[21] He C, Takeda T, Huang Z, Xu J, Chen J, Yi W, et al. Powder synthesis and luminescence of a novel yellow-emitting $Ba_5Si_{11}Al_7N_{25}:Eu^{2+}$ phosphor discovered by a single-particle-diagnosis approach for warm w-LEDs. Chem Eng J 2023;455(Pt 2):140932.
[22] Liu Y, Zhang R, Yan K, Sun JF. Ultrahighly efficient narrowband red luminescence of uniquely distorted Mn^{4+} octahedron in the feldspar-type LED phosphor. Laser Photonics Rev 2023;17(8):2200940.
[23] Jiang C, Peng M, Srivastava AM, Li L, Brik MG. Mn^{4+}-doped heterodialkaline fluorogermanate red phosphor with high quantum yield and spectral luminous efficacy for warm-white-light-emitting device application. Inorg Chem 2018;57(23):14705–14.
[24] Wang Y, Zhou Y, Ming H, Song E, Zhang C, Tang W, et al. Toward ultra-broadband absorption and high quantum efficiency red emission via fluoride single crystals with heavy Mn^{4+} doping. Laser Photonics Rev 2023;17(8):2300012.
[25] Feng L, Pi S, Zheng J, Liang W, Li J, Zhou T, et al. Realizing thermal and moisture stability in the $K_2Ge_{1-x}Ti_xF_6:Mn^{4+}$ red phosphors with high efficiency for WLEDs. Ceram Int 2023;49(16):27486–95.
[26] Pratama AW, Piluharto B, Widiastuti N, Mahardika M. The impact of nanoparticles on agriculture and soil, by Nar Singh Chauhan and Sarvajeet Singh Gill. Adv Agrochem 2024;3(4):261–2.
[27] Chen Y, Wu K, He J, Tang Z, Shi J, Xu Y, et al. A bright and moisture-resistant red-emitting $Lu_3Al_5O_{12}:Mn^{4+},Mg^{2+}$ garnet phosphor for high-quality phosphor-converted white LEDs. J Mater Chem C 2017;5(34):8828–35.
[28] Xia Z, Meijerink A. Ce^{3+}-doped garnet phosphors: composition modification, luminescence properties and applications. Chem Soc Rev 2017;46(1):275–99.
[29] Ju M, Zhong MM, Lu C, Yeung YY. Deciphering the microstructure and energy-level splitting of Tm^{3+}-doped yttrium aluminum garnet. Inorg Chem 2019;58(2):1058–66.
[30] Clark SJ, Segall MD, Pickard CJ, Hasnip PJ, Probert MIJ, Refson K, et al. First principles methods using CASTEP. Z Kristallogr Cryst Mater 2005;220(5–6):567–70.
[31] Chen D, Zhou Y, Xu W, Zhong J, Ji Z, Xiang W. Enhanced luminescence of Mn^{4+}: $Y_3Al_5O_{12}$ red phosphor via impurity doping. J Mater Chem C 2016;4(8):1704–12.
[32] Long J, Wang Y, Ma R, Ma C, Yuan X, Wen Z, et al. Enhanced luminescence performances of tunable $Lu_{3-x}Y_xAl_5O_{12}:Mn^{4+}$ red phosphor by ions of Rn^+ (Li^+, Na^+, Ca^{2+}, Mg^{2+}, Sr^{2+}, Sc^{3+}). Inorg Chem 2017;56(6):3269–75.
[33] Li D, Kou E, Li W, Zhang H, Zhang X, Zhuang J, et al. Oxidation-induced quenching mechanism of ultrabright red carbon dots and application in antioxidant RCDs/PVA film. Chem Eng J 2021;425:131653.
[34] Ben HN. Poly(vinyl alcohol): review of its promising applications and insights into biodegradation. RSC Adv 2016;6(46):39823–32.
[35] Nguyen SV, Lee BK. PVA/CNC/TiO_2 nanocomposite for food-packaging: improved mechanical, UV/water vapor barrier, and antimicrobial properties. Carbohydr Polym 2022;298:120064.
[36] Wang F, Wang M, Liu Y, Pu Y, Wang JX, Wang D, et al. Intensified synthetic approach for GdYAG:Ce phosphors with ultrahigh color rendering toward healthy lighting. AIChE J 2024;70(1):e18253.
[37] Wang Z, Ji H, Wang F, Hou X, Yi S, Zhou Y, et al. Valence state control of manganese in $MgAl_2O_4:Mn^{4+}$ phosphor by varying the Al_2O_3 crystal form. J Inorg Mater 2021;36(5):513–20.
[38] Bayer G. Vanadates $A_3B_2V_3O_{12}$ with garnet structure. J Am Ceram Soc 1965;48(11):600.
[39] Sharma SK, Lin YC, Carrasco I, Tingberg T, Bettinelli M, Karlsson M. Weak thermal quenching of the luminescence in the $Ca_3Sc_2Si_3O_{12}:Ce^{3+}$ garnet phosphor. J Mater Chem C 2018;6(33):8923–33.
[40] Wang Z, Cheng L, Tang H, Yu X, Xie J, Mi X, et al. Garnet type $Y_2Mg_3Ge_3O_{12}$: Dy^{3+}/Eu^{3+} phosphors excited near ultraviolet: luminescence properties and energy transfer mechanisms. J Solid State Chem 2021;301:122295.
[41] Toby BH. EXPGUI, a graphical user interface for GSAS. J Appl Crystallogr 2001;34(2):210.
[42] Gu S, Xia M, Zhou C, Kong Z, Molokeev MS, Liu L, et al. Red shift properties, crystal field theory and nephelauxetic effect on Mn^{4+}-doped $SrMgAl_{10-y}Ga_yO_{17}$ red phosphor for plant growth LED light. Chem Eng J 2020;396:125208.
[43] Adachi S. Crystal-field and Racah parameters of Mn^{4+} ion in red and deep red-emitting phosphors: fluoride versus oxide phosphor. J Lumin 2020;218:116829.
[44] Riseberg LA, Weber MJ. Spectrum and anomalous temperature dependence of the $^2E \rightarrow {}^4A_2$ emission of $Y_3Al_5O_{12}:Mn^{4+}$. Solid State Commun 1971;9(11):791–4.
[45] Tomiki T, Ganaha Y, Shikenbaru T, Futemma T, Yuri M, Aiura Y, et al. Optical spectra of $Y_3Al_5O_{12}$ (YAG) single crystals in the vacuum ultraviolet region. II. J Phys Soc Jpn 1993;62(4):1388–400.
[46] Kozuka S, Ueda J, Tanabe S. Multimodal deep red luminescent ratiometric thermometer of $LaAlO_3$ doped with Mn^{4+}. Physica B 2022;633:413492.
[47] de Wit JW, van Swieten TP, van de Haar MA, Meijerink A, Rabouw FT. Increasing the power: absorption bleach, thermal quenching, and auger quenching of the red-emitting phosphor $K_2TiF_6:Mn^{4+}$. Adv Opt Mater 2023;11(9):2202974.
[48] Senden T, van Dijk-Moes RJA, Meijerink A. Quenching of the red Mn^{4+} luminescence in Mn^{4+}-doped fluoride LED phosphors. Light Sci Appl 2018;7(1):8.
[49] Zhang M, Ming Y, Wang HB, Jin HL. Strategies for adaptation to high light in plants. aBIOTECH 2024;5(3):381–93.